Propagation of orientation uncertainty of 3D rigid object to its points

Marek Franaszek
National Institute of Standards and Technology
Gaithersburg, MD 20899, USA
marek@nist.gov

Geraldine S. Cheok
National Institute of Standards and Technology
Gaithersburg, MD 20899, USA
cheok@nist.gov

Abstract

If a CAD model of a rigid object is available, the location of any point on an object can be derived from the measured 6DOF pose of the object. However, the uncertainty of the measured pose propagates to the uncertainty of the point in an anisotropic way. We investigate this propagation for a class of systems that determine an object pose by using point-based rigid body registration. For such systems, the uncertainty in the location of the points used for registration propagates to the pose uncertainty. We find that for different poses of the object, the direction corresponding to the smallest propagated uncertainty remains relatively unchanged in the object's local frame, regardless of object pose. We show that this direction may be closely approximated by the moment of inertia axis which is based on the configuration of the fiducials. We use existing theory of rigid-body registration to explain the experimental results, discuss the limitations of the theory and practical implications of our findings.

1. Introduction

The pose of a rigid object is determined by six degrees of freedom (6DOF): three angles parametrizing the object orientation matrix $\boldsymbol{R}$ and three components of vector $\boldsymbol{\tau}$ defining the object's location. When the Computer Aided Design (CAD) model of an object is available, any Point of Interest (POI) on the object can be calculated using the 6DOF data obtained from pose measuring systems. It is then important to understand how uncertainty in the measured pose propagates to the uncertainty of a POI. In manufacturing, when rigid parts are assembled by autonomous robots, uncertainty in pose has to be propagated to the grasp points or points of contact between parts [1-4]. In peg-in-hole testing (routinely used to benchmark a robot's performance [5-8]) uncertainty in the hole location directly impacts the test outcome [9-13].

In [14] it was shown that object orientation uncertainty propagates to a POI in an anisotropic way (i.e., it depends on the direction in space) and the direction along which the propagated uncertainty is the smallest is determined by the eigenvector corresponding to the largest eigenvalue of the covariance matrix of orientation noise. Prior knowledge of this direction would be beneficial in planning assembly tasks but three issues need to be addressed. 1) It is not known if the direction of the relevant eigenvector is fixed in the local object coordinate frame, i.e. whether it depends on object orientation (large, unknown variations of the direction would negate any potential benefits of exploiting the anisotropic propagation of object orientation uncertainty). 2) Evaluating the covariance matrix of orientation noise is a time-consuming task which requires collection of many repeated measurements. Therefore, it would be helpful if the direction of the smallest propagated uncertainty could be estimated in a more efficient way. 3) In practical applications, the need for very accurate locations of different POIs may be required in an assembly process. To optimize process planning, users may need to know if the direction of the smallest propagated uncertainty can be controlled and changed based on the location of the POI. The objective of this study is to address these issues for a certain class of pose measuring systems.

Orientation components of pose are rarely measured directly, and in this paper, we investigate the class of pose measuring systems that acquire points (fiducial points) for rigid body registration to determine pose. Some systems use rigidly attached markers to the object or can automatically identify some characteristic points on the object. For these systems, the transformation $\{\boldsymbol{R}, \boldsymbol{\tau}\}$ is found by minimizing the Fiducial Registration Error *FRE*

$$FRE(\boldsymbol{R}, \boldsymbol{\tau}) = \sqrt{\frac{1}{J}\sum_{j=1}^{J}\left\|\boldsymbol{R}\boldsymbol{X}_j + \boldsymbol{\tau} - \boldsymbol{Y}_j\right\|^2} \qquad (1)$$

where $\{\boldsymbol{X}\}_J$ is a set of J fiducials measured in one coordinate frame (working frame, for example CAD frame or other predefined local frame) and $\{\boldsymbol{Y}\}_J$ is a set of corresponding fiducials measured in the second frame (destination frame, for example global or instrument's frame). Pose measuring systems track the movement of the object's frame, and the transformation $\{\boldsymbol{R}, \boldsymbol{\tau}\}$ defines the pose of the object in the instrument's frame. Once the transformation is known, it can be applied to any POI which was not used in the process of registration. Such a point (also called a target point) located at $\boldsymbol{U}$ may be used to calculate the Target Registration Error $TRE(\boldsymbol{U})$ which is defined as the distance

between the transformed target and its location in the instrument's frame.

Uncertainty in the locations of fiducials propagates to the transformation $\{\boldsymbol{R}, \boldsymbol{\tau}\}$ and, further, to the location of the transformed target. Thus, noise perturbing the locations of fiducials affects $TRE(\boldsymbol{U})$. Finding an analytic expression which relates $TRE(\boldsymbol{U})$ with the statistical properties of noise perturbing fiducials has been the subject of extensive research for many years [15-19]. The main conclusions from these studies can be summarized as follow: 1) $TRE(\boldsymbol{U})$ depends on the location of target $\boldsymbol{U}$ relative to the three main axes of the moment of inertia determined from the spatial configuration of fiducials $\{\boldsymbol{X}\}_J$; 2) $TRE(\boldsymbol{U})$ can be expressed as the sum of two components: one related to uncertainty in position $\boldsymbol{\tau}$ and the second related to uncertainty in the orientation data $\boldsymbol{R}$; 3) both components are proportional to the magnitude of noise; 4) the orientation component is anisotropic while the positional component is isotropic.

For the class of pose measuring systems which use point-based rigid body registration to determine the pose of a rigid object, uncertainty of any POI on that object will exhibit the properties of TRE described above. Thus, the propagation of the object orientation uncertainty to a POI should depend on the location of the fiducials. We verify this by acquiring different poses using a two-camera system and small spherical targets to get 6DOF data.

2. Background

Let column vector $\boldsymbol{U}$ define the location of a POI in the CAD coordinate frame and $\boldsymbol{u}$ be a unit vector parallel to $\boldsymbol{U}$ such that $\boldsymbol{U} = \|\boldsymbol{U}\|\,\boldsymbol{u}$. If $\boldsymbol{R}_n$ is the orientation matrix of a rigid object and $\boldsymbol{t}_n$ its location obtained from the *n*-th noisy measurement, then $\boldsymbol{U}_n$ is the location of the POI on the rotated object in the coordinate frame of the pose measuring instrument

$$\boldsymbol{U}_n = \|\boldsymbol{U}\|\,\boldsymbol{w}_n + \boldsymbol{t}_n \tag{2}$$

where $\boldsymbol{w}_n$ is a unit vector pointing to the rotated POI in the coordinate frame of the instrument

$$\boldsymbol{w}_n = \boldsymbol{R}_n\,\boldsymbol{u}\,. \tag{3}$$

In the rest of this paper, any unit column vector $\boldsymbol{a}$ will be parametrized by two spherical angles as

$$\boldsymbol{a}(\vartheta, \varphi) = [\cos\vartheta\cos\varphi, \cos\vartheta\sin\varphi, \sin\vartheta]^T. \tag{4}$$

We investigate the propagation of uncertainty of $\boldsymbol{R}_n$ to the uncertainty of $\boldsymbol{w}_n$. We assume that

$$\boldsymbol{R}_n = \boldsymbol{R}_{avg}\,\Delta\boldsymbol{R}_n \tag{5}$$

where $\boldsymbol{R}_{avg}$ is the averaged orientation obtained from *N* repeated measurements, $\Delta\boldsymbol{R}_n$ is a small random rotation (noise), and $n = 1, \ldots, N$. In axis-angle representation $(\boldsymbol{a}_n, \rho_n)$, the smallness of the random rotation is gauged by small values of angle ρ_n and this leads to the following expression for $\Delta\boldsymbol{R}_n$ in linear approximation

$$\Delta\boldsymbol{R}_n(\boldsymbol{a}_n, \rho_n) \approx \boldsymbol{I} + \begin{bmatrix} 0 & -q_{z,n} & q_{y,n} \\ q_{z,n} & 0 & -q_{x,n} \\ -q_{y,n} & q_{x,n} & 0 \end{bmatrix} \tag{6}$$

where $\boldsymbol{I}_{3\times3}$ is the identity matrix, $\boldsymbol{a}_n$ is a unit vector defining the axis of rotation, and

$$\boldsymbol{q}_n = \rho_n\,\boldsymbol{a}_n\,. \tag{7}$$

The covariance matrix $\boldsymbol{C}(\boldsymbol{q})$ of the orientation data is then given by

$$\boldsymbol{C}(\boldsymbol{q}) = \tfrac{1}{N}[\boldsymbol{q}_1, \ldots, \boldsymbol{q}_N][\boldsymbol{q}_1, \ldots, \boldsymbol{q}_N]^T\,. \tag{8}$$

Repeated measurements of the orientation matrix $\boldsymbol{R}_n$ in (3) yield a corresponding set of unit vectors $\{\boldsymbol{w}\}_N$ which are tightly distributed around the average direction $\boldsymbol{w}_{avg}$. If μ denotes the angle between $\boldsymbol{w}_n$ and $\boldsymbol{w}_{avg}$, then its distribution can be described by the Fisher-Bingham-Kent (FBK) distribution $G_{\sigma,\beta}(\mu)$ [20-22]. FBK has two parameters: angular uncertainty σ and eccentricity parameter β. Larger values of σ indicate larger deviations of $\boldsymbol{w}_n$ from $\boldsymbol{w}_{avg}$(i.e., more noisy data). Larger values of β correspond to a more elongated elliptical contour of constant probability on the (ϑ, φ) plane (as $\beta \to 0$, the contour approaches a circle).

If the orientation matrices $\boldsymbol{R}_n$ are obtained by pose measuring systems which derive orientation from a set of measured fiducial markers and use the rigid-body, point-based registration, then there are equations which provide σ for certain types of noise disturbing the locations of fiducials. For example, for Gaussian, homogenous and anisotropic noise (covariance matrix $\boldsymbol{\Psi}$ is the same at each point in space but the three variances, i.e. eigenvalues of $\boldsymbol{\Psi}$, substantially differ from each other) an expression for $TRE(\boldsymbol{U})$ is provided in [23]. To study the component of TRE which depends on direction only, the isotropic part of TRE and the linear dependence on the distance of the POI to the origin are ignored (i.e., vector $\boldsymbol{U}$ is replaced by the unit vector $\boldsymbol{u} = [u_1, u_2, u_3]^T$). Then, the variance σ^2 of the deviation angles μ between instantaneous vectors $\boldsymbol{w}_n$ in (3) and their mean $\boldsymbol{w}_{avg}$ is given by

$$\sigma^2(\boldsymbol{u}) = \sum_{i=1}^{3}\sum_{j\neq i}^{3}\left[\frac{u_j^2\left(\Lambda_j^2\Psi_{i,i} + \Lambda_i^2\Psi_{jj}\right)}{\left(\Lambda_i^2 + \Lambda_j^2\right)^2} + \sum_{k\neq i,j}^{3} s_{i,j,k}\right] \tag{9}$$

where

$$s_{i,j,k} = u_j u_k \Psi_{j,k}\,\frac{\Lambda_i^2}{\left(\Lambda_i^2+\Lambda_j^2\right)\left(\Lambda_i^2+\Lambda_k^2\right)}\,. \tag{10}$$

Parameters Λ_i can be calculated from the Singular Value Decomposition (SVD) of the matrix $[\boldsymbol{X}]_J = [\boldsymbol{X}_1, \ldots, \boldsymbol{X}_J]$ where column vector $\boldsymbol{X}_j$ is the location of the *j*-th fiducial in the CAD coordinate frame. Thus,

$$[\boldsymbol{X}]_J = \boldsymbol{U}_X\boldsymbol{\Lambda}\boldsymbol{V}^T \tag{11}$$

where the diagonal matrix $\boldsymbol{\Lambda} = diag(\Lambda_1, \Lambda_2, \Lambda_3)$ and $\boldsymbol{U}_X$ is the rotation matrix which aligns axes of $[\boldsymbol{X}]_J$ with the CAD frame axes. The three columns of $\boldsymbol{U}_X$ also define the eigenvectors $[\boldsymbol{m}_{min}, \boldsymbol{m}_{mid}, \boldsymbol{m}_{max}]$ of the moment of inertia

matrix $\boldsymbol{M}$ where

$$\boldsymbol{M} = trace(\boldsymbol{covX})\,\boldsymbol{I} - \boldsymbol{covX} \quad (12)$$

and the covariance matrix $\boldsymbol{covX}_{3\times3} = \boldsymbol{cov}([\boldsymbol{X}]_J^T)$. Eigenvalues $[h_{min}, h_{mid}, h_{max}]$ of $\boldsymbol{M}$ are equal

$$(J-1)[\Lambda_2^2+\Lambda_3^2,\ \Lambda_3^2+\Lambda_1^2,\ \Lambda_1^2+\Lambda_2^2] \quad (13)$$

where h_{min} corresponds to the largest while h_{max} to the smallest element of $\boldsymbol{\Lambda}$, as follows from (12).

Note that in (9) and (10) only elements of the diagonal matrix $\boldsymbol{\Lambda}$ are used while covariance of noise $\boldsymbol{\Psi}$ may have non-zero off-diagonal elements. This is a consequence of the fact that the orientation of the noise matrix is independent of the orientation of $\boldsymbol{M}$ matrix (i.e., spatial configuration of fiducials). Thus, for any arbitrary orientation of a rigid object, three major axes of the moment of inertia may be aligned with the rotated CAD frame axes (by using rotation $\boldsymbol{U}_X$) but it will not lead to alignment of noise matrix $\boldsymbol{\Psi}$ with CAD frame.

3. Experiment Description

The 6DOF pose measurements were obtained using an OptiTrack Duo system which is a two-camera, motion capture system [24]. The system locates small spherical markers covered with reflective material in its work volume and finds the centers of these spheres. A group of markers attached to a rigid object forms a configuration of fiducials. When the new configuration is created, the measured locations of the markers at that time define the initial object pose. Thus, the system tracks the motion of the object by tracking these markers. It uses a rigid-body, point-based registration (i.e., it minimizes FRE in (1)) to calculate the current pose of an object relative to its initial pose. As the object moves, some markers are occluded, but the system tracks the visible markers and use them to determine the object pose. The system outputs four components of a unit quaternion and three components of the positional part of the 6DOF pose data. In addition to object pose, *xyz*-locations of each visible marker are also provided.

In the experiment, spherical markers were glued to a rigid object (a piece of aluminum rail). The total of $M = 15$ randomly selected poses were measured using two different configurations of markers. For poses $m = 1$ to 5, the same configuration consisting of $J = 5$ markers was used. For poses $m = 6$ to 15, the configuration consisting of $J = 7$ markers was used. At each m-th pose, a large number $N \gtrsim 50{,}000$ of repeated measurements were obtained.

Figure 1 shows fifteen average measured poses $\boldsymbol{R}_{avg}(m)$ together with locations of fiducials. For poses $m = 1$ and $m = 6$, the new configurations of fiducials are defined and therefore the corresponding orientations $\boldsymbol{R}_{avg}(m) = \boldsymbol{I}$. Black dots represent fiducials which were not visible at a given pose and the number of undetected fiducials is provided for each pose. The same fiducials were undetected for pairs of poses: $m =$ (4,5), (9,10), (8,14).

4. Data processing

For each data file containing N repeated measurements, the average rotation $\boldsymbol{R}_{avg}$ in (5) was calculated first. There are different ways of calculating the average rotation and not all of them are correct. In this study, we used the mean rotation in the Euclidean sense [25]. Once the average rotation was determined, small random rotations $\Delta\boldsymbol{R}_n$ were calculated from (5), i.e.

$$\Delta\boldsymbol{R}_n = \boldsymbol{R}_{avg}^T\boldsymbol{R}_n \quad (14)$$

where we used the property that the inverse of rotation matrix is equal to the transposed matrix, $\boldsymbol{R}^{-1} = \boldsymbol{R}^T$. Calculating small rotations from experimental data requires extra caution. The data file contained four components of unit quaternion $\boldsymbol{g}_n$ which can be converted to the rotation matrix $\boldsymbol{R}(\boldsymbol{g}_n)$. However, we noticed that due to truncation error in the stored values of $\boldsymbol{g}_n$ (six decimal digits), the resulting matrix was not orthonormal, i.e. $\boldsymbol{R}(\boldsymbol{g}_n)\,\boldsymbol{R}^T(g_n) \neq \boldsymbol{I}$. This caused the resulting matrix on the left side of (14) to also violate orthonormality and linear approximation in (6) yielding incorrect orientation noise $\boldsymbol{q}$. To overcome this problem, we determined the rotation matrix $\boldsymbol{R}_n$ directly by minimizing FRE in (1). Specifically, for pose $m = 1$ when the configuration of five fiducials was defined, we calculated the mean locations of fiducials $\{\overline{\boldsymbol{X}}\}_J$ from N repeated measurements. Then, for poses $m = 2, \ldots, 5$, for each repeated n-th measurement of fiducials, the registration between $\{\overline{\boldsymbol{X}}\}_{J(m)}$ and $\{\boldsymbol{Y}\}_{J(m),n}$ was performed and the corresponding rotation matrix $\boldsymbol{R}_n$ was calculated as in [26]. The matrix determined in this manner satisfied the condition of orthonormality, ensuring that linear approximation in (6) yielded the correct orientation noise $\boldsymbol{q}$. The same procedure was repeated for pose $m = 6$ when the new configuration with seven fiducials was defined and registration between new $\{\overline{\boldsymbol{X}}\}_{J(m)}$ and $\{\boldsymbol{Y}\}_{J(m),n}$ was performed for poses $m = 7, \ldots, 15$. Due to marker occlusions, different poses used different subsets of the fiducials, and the registrations were performed using varying number of fiducials $J(m)$.

Once rotations $\boldsymbol{R}_n, n = 1, \ldots, N$ were calculated from the experimental data, a set of unit vectors $\{\boldsymbol{w}\}_N$ in (3) was formed for a unit vector $\boldsymbol{u}(\vartheta, \varphi)$ parametrized by two angles as in (4). For each set $\{\boldsymbol{w}\}_N$, two parameters of FBK distribution, $\sigma(\vartheta, \varphi)$ and $\beta(\vartheta, \varphi)$ were determined as in [21]. The calculations were repeated on a grid of angles $[-90°\ 90°] \times [0°\ 360°]$ so that the angular uncertainty σ could be displayed on a unit sphere. In addition, for some selected unit vectors $\boldsymbol{u}$, the histograms of deviation angles μ_n between $\boldsymbol{w}_n$ and $\boldsymbol{w}_{avg}$ were constructed.

For each m-th pose, the average rotation $\boldsymbol{R}_{avg}(m)$ was evaluated and small random rotations $\Delta\boldsymbol{R}_n$ were determined as in (14). From each $\Delta\boldsymbol{R}_n$, the corresponding noisy orientation perturbation $\boldsymbol{q}_n$ was extracted using (6) and from (7) the axis of small random rotation $\boldsymbol{a}_n$ was obtained.

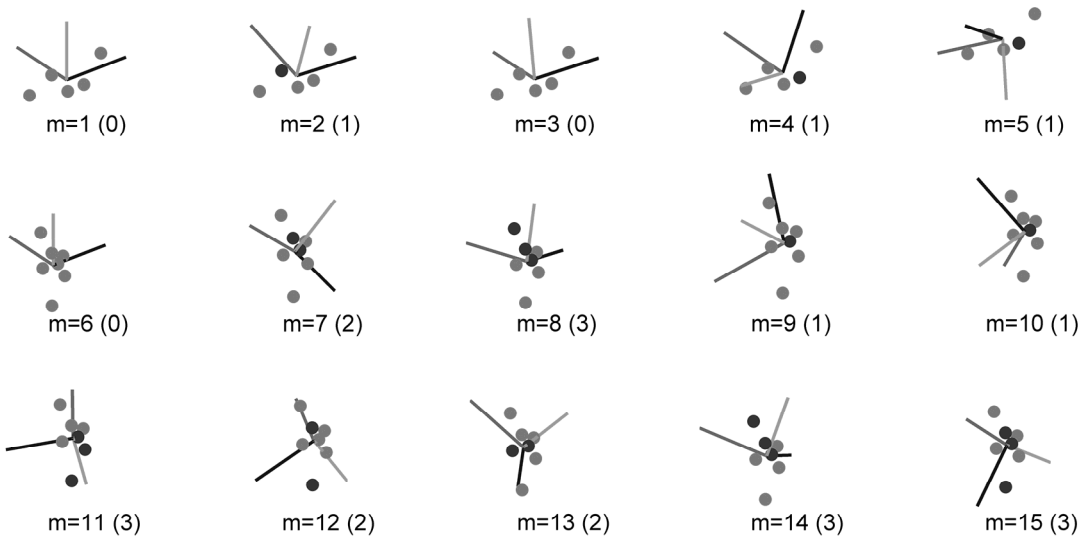

Figure 1. Fifteen measured poses $\boldsymbol{R}_{avg}(m)$ where dots represent the fiducial locations. Gray dots are visible fiducials, and black dots are occluded fiducial(s); numbers in parenthesis provide the total number of occluded fiducials. Configurations of fiducials for rigid-body registration were defined in poses m = (1,6) and, therefore, the corresponding rotations $\boldsymbol{R}_{avg} = \boldsymbol{I}$.

The axis is a unit vector which can be parametrized as in (4) so a histogram of axes $\boldsymbol{a}_n(\vartheta_n, \varphi_n)$ could be displayed on a unit sphere using a grid of angles, similar to uncertainty $\sigma(\vartheta, \varphi)$. Once all N random orientation perturbations $\{\boldsymbol{q}\}_N$ were calculated for the m-th pose, their covariance matrix $\boldsymbol{C}(\boldsymbol{q})$ was determined as in (8). Then, its eigenvalues $[l_{min}, l_{mid}, l_{max}]$ and the corresponding eigenvectors $[\boldsymbol{c}_{min}, \boldsymbol{c}_{mid}, \boldsymbol{c}_{max}]$ were calculated.

For pose $m = 1$, SVD of the full configuration of $J = 5$ average locations of fiducials $[\overline{\boldsymbol{X}}]_J$ was performed as in (11). Then, for poses $m = 2, \ldots, 5$, the corresponding subset of fiducials detected by cameras was identified and SVD of that subset $[\overline{\boldsymbol{X}}]_{J(m)}$ was performed. The same procedure was repeated for pose $m = 6$ (where the full configuration consisted of $J = 7$ fiducials) and the remaining poses $m = 7, \ldots, 15$. Thus, for each m-th pose, the corresponding diagonal matrix $\boldsymbol{\Lambda}(m)$ and orthonormal matrix $\boldsymbol{U}_X(m)$ in (11) was determined. Similar calculations could be done for the moment of inertia matrix $\boldsymbol{M}(m)$, yielding equivalent results as follows from (12) and (13). We note that eigenvectors are defined in the object's local frame and in the instrument's coordinate frame they follow exactly the m-th orientation of the object $\boldsymbol{R}_{avg}(m)$ if the same set of fiducials is detected in each m-th pose. Thus, for the instruments which cannot detect all fiducials for every pose, the moment of inertia and its eigenvectors will be varying.

To study the consequences of misalignment between the moment of inertia matrix and the covariance matrix of noisy fiducials, equations (9) and (10) were used for a fixed configuration of fiducials (fixed $\boldsymbol{\Lambda}$ in (11)) and different noise covariance matrices $\boldsymbol{\Psi}$. Specifically, noise matrix was set to

$$\boldsymbol{\Psi}(\omega) = \boldsymbol{R}(\boldsymbol{a}, \omega)\, \boldsymbol{\Psi}_0\, \boldsymbol{R}(\boldsymbol{a}, -\omega) \qquad (15)$$

where $\boldsymbol{\Psi}_0$ was a diagonal matrix and $\boldsymbol{R}(\boldsymbol{a}, \omega)$ was a rotation matrix in the (axis, angle) representation (we used the property that $\boldsymbol{R}^{-1}(\boldsymbol{a}, \omega) = \boldsymbol{R}(\boldsymbol{a}, -\omega)$). For $\omega = 0$, matrix $\boldsymbol{\Psi} = \boldsymbol{\Psi}_0$ and all off-diagonal elements $\Psi_{j,k} = 0$ in (10). This case corresponds to rather exceptional configuration in which the object is rotated in such manner that the axes of moment of inertia are aligned with the eigenvectors of the covariance matrix of the noise. As angle ω is gradually increased (i.e., the object is gradually turned away from the exceptional configuration) absolute values of the off-diagonal elements $|\Psi_{j,k}|$ also increase. Then, depending on the values of the elements of the diagonal matrices $\boldsymbol{\Lambda}$ and $\boldsymbol{\Psi}_0$, the locations of the extreme points of angular uncertainty $\sigma(\vartheta, \varphi)$ may move on a unit sphere (recall that a unit vector $\boldsymbol{u}$ in (9) can be parametrized by two angles as in (4)). Note that for perfectly isotropic noise, i.e. $\boldsymbol{\Psi}_0 = \psi \boldsymbol{I}$, off-diagonal elements $\Psi_{j,k}$ will always be zero, regardless of object orientation.

5. Results

Figure 2 shows the directions associated with the largest and the smallest principal moment of inertia $\boldsymbol{M}$. For poses $m = 6, \ldots, 15$, directions associated with the smallest moment of inertia (shown as solid, black lines) form four groups. For five of the poses, the directions overlap almost

exactly; for the remaining five poses, four have three occluded fiducials (poses $m = 8,11,14,15$). All lines are plotted in the coordinate frame associated with the first pose $m = 1$.

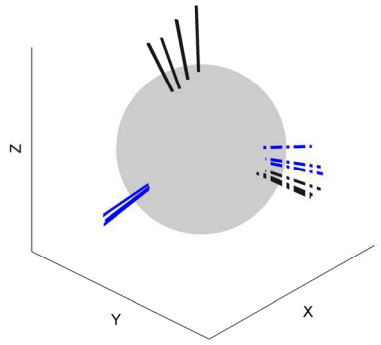

Figure 2. Directions associated with the smallest principal moment of inertia $\boldsymbol{M}$ (eigenvector $\boldsymbol{m}_{min}$, solid lines) and the largest one (eigenvector $\boldsymbol{m}_{max}$, dashed lines). Blue color marks poses $m = 1, \dots, 5$ while black marks poses $m = 6, \dots, 15$.

Figure 3 shows the histograms of the orientation noise $\boldsymbol{q}$ defined in (7) obtained from data acquired for pose $m = 5$. Similar distributions were observed for the other poses. Figure 4 shows the histograms of deviation angles μ_n between the mean $\boldsymbol{w}_{avg}$ and noisy rotated unit vectors $\boldsymbol{w}_n$ defined in (3). The two histograms correspond to two different choices of vector $\boldsymbol{u}$ in (3) which is rotated by noisy rotations $\boldsymbol{R}_n$: one is aligned with the direction in which propagated uncertainty σ is the largest (i.e., $\boldsymbol{c}_{min}$), the other is aligned with the direction where the propagated uncertainty is the smallest ($\boldsymbol{c}_{max}$). In addition, for each set of rotated noisy vectors $\{\boldsymbol{w}\}_N$, two parameters of FBK distribution (i.e., orientation uncertainty σ and eccentricity β) are calculated. The corresponding values are $\sigma = (0.161,\ 0.019)$ [mrad] and $\beta = (15.4, 1334.2)$ [mrad^{-2}] for the direction of the largest and the smallest propagated uncertainty, respectively. Once both parameters σ and β are known, the theoretical distribution FBK of the deviation angles μ can be plotted. The experimental histograms and theoretical FBK distributions displayed in Figure 4 were obtained from data acquired in pose $m = 10$, corresponding plots obtained for other poses are similar.

Figure 5 shows the histograms of the spherical angles (ϑ_n, φ_n) parametrizing (as in (4)) the rotated noisy unit vectors $\boldsymbol{w}_n$ defined in (3) which were used to create the plots in Figure 4. The histograms are centered at angles $(\vartheta_{avg}, \varphi_{avg})$ which parametrize the mean unit vector $\boldsymbol{w}_{avg}$, so $\Delta\vartheta_n = \vartheta_n - \vartheta_{avg}$ and $\Delta\varphi_n = \varphi_n - \varphi_{avg}$.

In Figure 6 histograms of axes $\boldsymbol{a}_n$ of small random rotations $\Delta\boldsymbol{R}_n(\boldsymbol{a}_n, \rho_n)$ defined in (6) are shown. In addition, the eigenvectors corresponding to the largest and the smallest eigenvalue of the covariance matrix of orientation noise $\boldsymbol{C}(\boldsymbol{q})$ given by (8) and the moment of inertia matrix $\boldsymbol{M}$ defined in (12) are plotted. Histograms were obtained from data acquired in poses $m = (8, 14)$. For that poses, the same subset of $J = 5$ fiducials was detected and used to perform rigid-body registration. Both graphs are plotted from the same view angle in the object's coordinate frame associated with the full configuration of seven fiducials (pose $m = 6$).

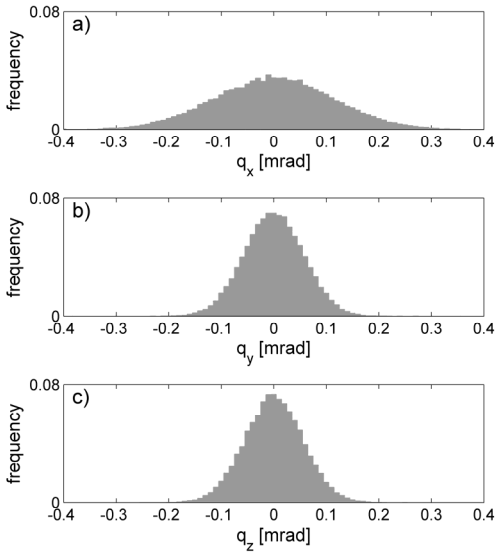

Figure 3. Histogram of orientation noise $\boldsymbol{q} = [q_x, q_y, q_z]$ calculated from small random rotations $\Delta\boldsymbol{R}_n(\boldsymbol{q})$ in (6) and (14).

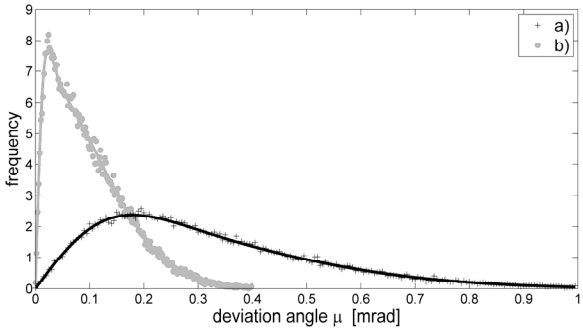

Figure 4. Histograms of the angles of deviation μ (markers) and the corresponding theoretical FBK distributions (solid lines) for two different directions of vector $\boldsymbol{u}$ in (3): a) $\boldsymbol{u}$ aligned with the eigenvector $\boldsymbol{c}_{min}$ of the covariance matrix $\boldsymbol{C}(\boldsymbol{q})$; b) $\boldsymbol{u}$ aligned with $\boldsymbol{c}_{max}$.

In Figure 7, the angular dependence of the orientation uncertainty $\sigma(\vartheta, \varphi)$ is shown for the same poses as in Figure 6, i.e. $m = (8, 14)$. Eigenvectors corresponding to the largest and the smallest eigenvalue of covariance matrix $\boldsymbol{C}(\boldsymbol{q})$ are plotted for each data set (black solid and dashed lines, respectively) and eigenvectors corresponding to the smallest and the largest eigenvalue of the moment of inertia matrix $\boldsymbol{M}$ are plotted (grey solid and dashed lines,

respectively). The plots in Figure 7 are displayed in the same coordinate frame and from the same view angle as the plots in Figure 6, so the directions of the axes in both figures are the same.

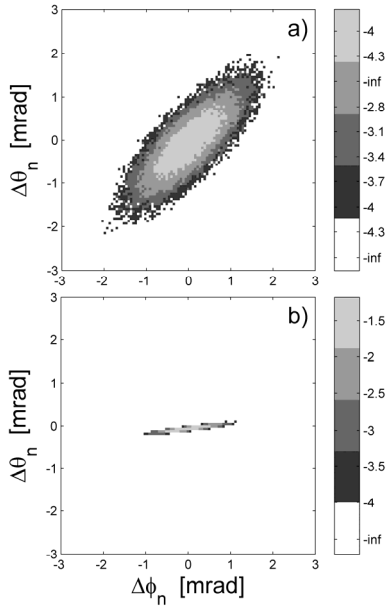

Figure 5. Histograms (plotted in log scale) of the spherical angles (ϑ_n, φ_n) parametrizing the same unit vectors $\boldsymbol{w}_n$ which were used to create the plots in Figure 4: a) $\boldsymbol{u}$ aligned with the eigenvector $\boldsymbol{c}_{min}$; b) $\boldsymbol{u}$ aligned with $\boldsymbol{c}_{max}$. *-inf* indicates empty bins.

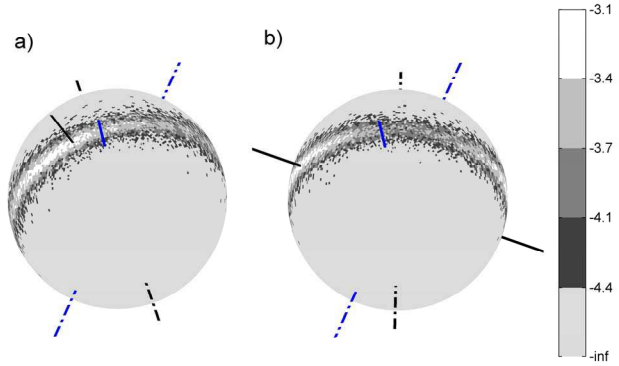

Figure 6. Histograms of axes $\boldsymbol{a_n}(\vartheta_n, \varphi_n)$ of small random rotations (plotted in log scale) for pose: a) $m = 8$; b) $m = 14$. Black lines show directions of eigenvectors of covariance matrix $\boldsymbol{C}(\boldsymbol{q})$: solid lines correspond to $\boldsymbol{c}_{max}$ and dashed line to $\boldsymbol{c}_{min}$. Blue lines indicate eigenvectors of the moment of inertia $\boldsymbol{M}$: solid lines correspond to $\boldsymbol{m}_{min}$ while dashed lines correspond to $\boldsymbol{m}_{max}$. *-inf* indicates empty bins, bin size $[1° \times 2°]$.

Plots similar to Figure 7 are shown in Figure 8 for data acquired in poses $m = (4, 9)$. However, the graph presented in a) is displayed in the coordinate frame associated with the full configuration of $J = 5$ fiducials defined in pose $m = 1$ while the graph in b) in coordinate frame associated with the full configuration of $J = 7$ fiducials defined in pose $m = 6$. Also, different view angles are used to ensure a clear view of relevant features (i.e., misalignment of solid black and grey lines).

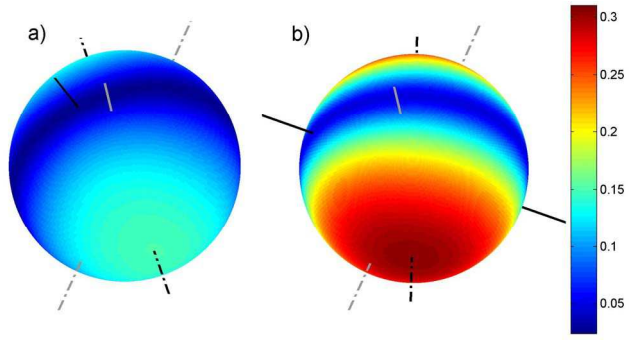

Figure 7. Angular distribution of orientation uncertainty $\sigma(\vartheta, \varphi)$ in [mrad] for data acquired in pose: a) $m = 8$; b) $m = 14$. Black lines show directions of eigenvectors of $\boldsymbol{C}(\boldsymbol{q})$: solid lines correspond to $\boldsymbol{c}_{max}$ and dashed lines to $\boldsymbol{c}_{min}$. Grey lines indicate eigenvectors of $\boldsymbol{M}$: solid lines correspond to $\boldsymbol{m}_{min}$ while dashed lines correspond to $\boldsymbol{m}_{max}$.

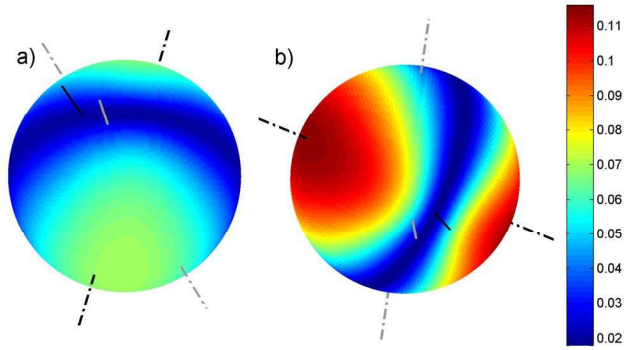

Figure 8. Angular distribution of orientation uncertainty $\sigma(\vartheta, \varphi)$ in [mrad] for data acquired in pose: a) $m = 4$; b) $m = 9$. Black lines show directions of eigenvectors of $\boldsymbol{C}(\boldsymbol{q})$: solid lines correspond to $\boldsymbol{c}_{max}$ and dashed lines to $\boldsymbol{c}_{min}$. Grey lines indicate eigenvectors of $\boldsymbol{M}$: solid lines correspond to $\boldsymbol{m}_{min}$ while dashed lines correspond to $\boldsymbol{m}_{max}$.

In Figure 9, misalignment angles between eigenvectors of the covariance matrix $\boldsymbol{C}(\boldsymbol{q})$ and the corresponding eigenvectors of the moment of inertia matrix $\boldsymbol{M}$ are plotted for all poses excluding poses for $m = (1, 6)$ which were used as reference poses. In Figure 9a, α_{max} is the angle between the eigenvector $\boldsymbol{c}_{max}$ of $\boldsymbol{C}(\boldsymbol{q})$ and the eigenvector $\boldsymbol{m}_{min}$ of $\boldsymbol{M}$. In Figure 9b, α_{min} is the angle between the eigenvector $\boldsymbol{c}_{min}$ of $\boldsymbol{C}(\boldsymbol{q})$ and one of the eigenvectors $(\boldsymbol{m}_{mid}, \boldsymbol{m}_{max})$ whichever is closer to $\boldsymbol{c}_{min}$. In Figure 9c, α_{mid} is the angle between the eigenvector $\boldsymbol{c}_{mid}$ of $\boldsymbol{C}(\boldsymbol{q})$ and the remaining third eigenvector of the matrix $\boldsymbol{M}$.

Noise characteristics of the measured fiducial locations

were obtained by calculating the covariance matrix for each visible fiducial in each pose (total of 72 locations). Eigenvalues $\boldsymbol{\lambda} = [\lambda_{min}^2, \lambda_{mid}^2, \lambda_{max}^2]$ of each matrix were calculated and the magnitude of the noise $\kappa = \sqrt{trace(\boldsymbol{\lambda})}$ and the measure of noise anisotropy $\nu = \lambda_{max}/\lambda_{min}$ were determined. The median and the largest magnitude were $\kappa_{med} = 0.0375$ [mm] and $\kappa_{max} = 0.1726$ [mm]. For anisotropy, the corresponding characteristics were $\nu_{med} = 10.4$ and $\nu_{max} = 18.7$.

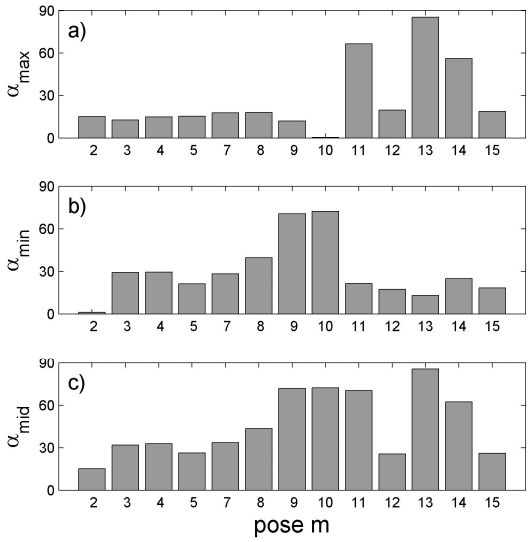

Figure 9. Misalignment angles between the eigenvectors of the covariance matrix $\boldsymbol{C}(\boldsymbol{q})$ and the eigenvectors of the moment of inertia matrix $\boldsymbol{M}$ for different poses; see text for definitions of three displayed angles (shown here in degrees).

6. Discussion

Repeated N measurements of object pose yield bell shaped, Gaussian like distribution of orientation noise $\boldsymbol{q}$, as shown in Figure 3. The resulting uncertainty in the object orientation propagates to a POI on the object. This propagation appears to be anisotropic, dependent on the unit vector $\boldsymbol{u}(\vartheta, \varphi)$ pointing in the direction of the POI in the object's local coordinate frame (CAD frame). In extreme cases, when $\boldsymbol{u}$ is aligned with the eigenvectors corresponding to the largest or the smallest eigenvalue of the covariance matrix of orientation noise $\boldsymbol{C}(\boldsymbol{q})$, the resulting uncertainties of the POI may be vastly different, as seen in Figure 4 and Figure 5. Such characteristics of pose measuring systems may impact processes which rely on 6DOF data acquired by these systems, for example part assembly in manufacturing. For systems which derive pose from raw measurements of fiducial markers attached to a rigid object, existing theoretical results provide a link between the properties of the covariance matrix $\boldsymbol{C}(\boldsymbol{q})$, propagated orientation uncertainty $\sigma(\vartheta, \varphi)$ and the placement of markers on or around the measured rigid object. The spatial configuration of fiducials is characterized by its moment of inertia $\boldsymbol{M}$ and the eigenvectors of $\boldsymbol{C}(\boldsymbol{q})$ and $\boldsymbol{M}$ are parallel for isotropic noise, i.e., $\Psi_{j,k} = 0$ in (10).

In our experiments, two different configurations of fiducials were defined: in pose $m = 1$ and pose $m = 6$. These two configurations yielded major axes of the moment of inertia $\boldsymbol{M}$ rotated relative to each other by roughly 90° around Y axis, see blue and black solid lines shown in Figure 2 (this can be understood by looking at actual placement of fiducials in Figure 1 for $m = 1$ and $m = 6$). However, different definitions of the full configuration of fiducials are not the only reason for the observed variability in the orientation of the major axes of $\boldsymbol{M}$. The instrument which we used in our experiment cannot detect all fiducials in every measured pose, see Figure 1. This implies that even for the same nominal configuration of fiducials different moments of inertia could be observed in different poses as different subsets of fiducials are used for rigid-body registration. Thus, the location of a POI relative to the major axes of $\boldsymbol{M}$ depends indirectly on object orientation as does the uncertainty of that POI propagated from the object pose uncertainty. We recall that covariance matrix $\boldsymbol{C}(\boldsymbol{q})$ is calculated from the set of vectors $\{\boldsymbol{q}\}_N$ and each $\boldsymbol{q}_n$ is parallel to its respective axis $\boldsymbol{a}_n$ of small random rotation $\Delta\boldsymbol{R}_n(\boldsymbol{a}_n, \rho_n)$, as follows from (7). Thus, the eigenvector $\boldsymbol{c}_{max}$ of $\boldsymbol{C}(\boldsymbol{q})$ defines the direction with the highest concentration of axes $\boldsymbol{a}_n$, i.e. the spot on a unit sphere where histogram of axes $\boldsymbol{a}_n$ reaches its maximum, see Figure 6. Similarly, $\boldsymbol{c}_{min}$ defines the direction in which the concentration of axes $\boldsymbol{a}_n$ is minimum. Furthermore, any rotation has the largest impact on vectors perpendicular to its axis of rotation and has no impact on vectors parallel to the axis. Therefore, the uncertainty σ (which accounts for the spread of vectors $\boldsymbol{w}_n$ around their mean $\boldsymbol{w}_{avg}$ in (3)) is the smallest in the direction defined by $\boldsymbol{c}_{max}$ and the largest in the direction aligned with $\boldsymbol{c}_{min}$, see Figure 7 and Figure 8. Thus, the eigenvectors of $\boldsymbol{C}(\boldsymbol{q})$ depend on the object orientation and so do $\sigma_{min}(\boldsymbol{c}_{max})$ and $\sigma_{max}(\boldsymbol{c}_{min})$. If the configuration of the fiducials does not change, the moment of inertia $\boldsymbol{M}$ is fixed and variations of $\boldsymbol{c}_{max}$ in the local object's frame would be small.

However, the variability in the directions of the major axes of $\boldsymbol{M}$ only partially explains why eigenvectors of $\boldsymbol{C}(\boldsymbol{q})$ depend on the object orientation. For example, the misalignment angle α_{max} between $\boldsymbol{c}_{max}$ and $\boldsymbol{m}_{min}$ is small for pose $m = 8$ in Figure 7a and large for pose $m = 14$ in Figure 7b (solid black and grey lines) although the same subset of fiducials was used to perform registration for both poses. Furthermore, for pose $m = 4$ in Figure 8a and pose $m = 9$ in Figure 8b both misalignments between $\boldsymbol{c}_{max}$ and $\boldsymbol{m}_{min}$ are small, although different subsets of fiducials were used for registration, see Figure 1. As shown in Figure 9, for most poses (except for poses $m = 11, 13, 14$) angle

$\alpha_{max} < 15°$ while the other two misalignment angles α_{mid} and α_{min} are larger. Thus, another factor must be responsible for the observed dependence of $\boldsymbol{C}(\boldsymbol{q})$ on object pose. We note that noise perturbing fiducials is strongly anisotropic, i.e., $\Psi_{j,k} \neq 0$ in (10). This means that for different object orientations in the instrument frame, different degrees of misalignment between the covariance of fiducial noise $\boldsymbol{\Psi}$ and matrix $\boldsymbol{M}$ are expected. This impacts uncertainty σ as shown in Figure 10 where theoretical model (9) of σ for homogenous and anisotropic noise affecting fiducials is plotted for increasing misalignment angle ω in (15). (Arbitrary axis of rotation $\boldsymbol{a}$ in (15) was used and diagonal noise matrix $\boldsymbol{\Psi}_0 = diag(13, 17, 1080)$ [μm^2], diagonal matrix $\boldsymbol{\Lambda}$ in (9) equal to $diag(160,\ 81, 17)$ [mm].) Experimental noise in fiducials is strongly non-homogeneous and therefore the theoretical σ does not exactly replicate experimental σ (compare Figure 10 with Figure 7 and Figure 8). Nevertheless, the angle α_{min} between the dashed black and grey lines in Figure 10 clearly increases with the increasing angle ω (i.e., increasing absolute values of off-diagonal elements of noise matrix $|\Psi_{j,k}|$ in (10)).

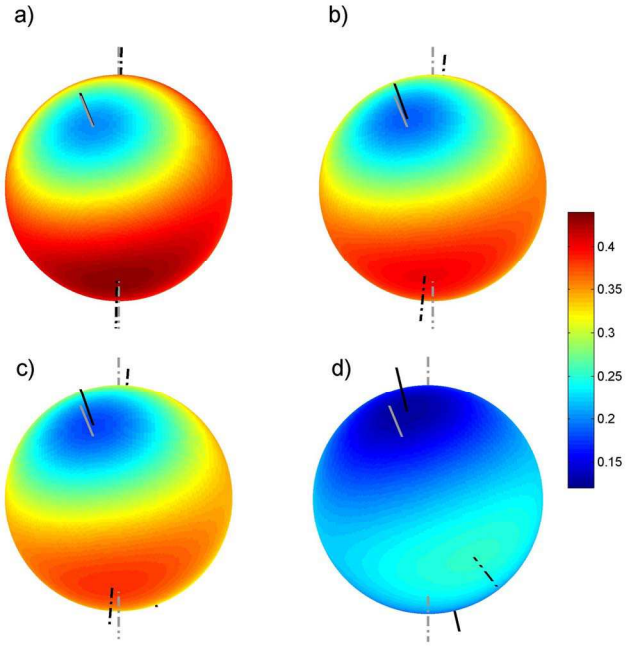

Figure 10. Theoretical uncertainty $\sigma(\vartheta, \varphi)$ in [mrad] from (9) for different noise covariance matrix $\boldsymbol{\Psi}(\omega)$ from (15): a) $\omega = 5°$; b) $\omega = 40°$; c) $\omega = 50°$; d) $\omega = 110°$. Black lines show directions where σ is the smallest (solid lines) and the largest (dashed lines). Grey solid lines are aligned with $\boldsymbol{m}_{min}$ and grey dashed lines with $\boldsymbol{m}_{max}$.

In summary, the direction along which the propagated uncertainty is the smallest corresponds to the eigenvector associated with the largest eigenvalue of the covariance matrix of orientation data. For the class of instruments investigated in this study, this direction is closely aligned to the direction of the axis corresponding to the smallest moment of inertia, for most of the measured object orientations. Even for poses $m = (11, 13, 14)$ where the misalignment angle α_{max} is large, as shown in Figure 9a, $\boldsymbol{m}_{min}$ points in the direction where the propagated to POI uncertainty σ is still small, see Figure 7b. This feature has a practical consequence: if a given POI is important, it is possible to attach fiducial markers to the rigid object so that the resulting axis of the smallest moment of inertia is aligned with the direction of the vector pointing to the POI. This will ensure that the POI will be in the area of the smallest possible uncertainty. If the propagated uncertainty needs to be minimized for different POIs on the same object, the system may dynamically select different subsets of fiducials to ensure that each POI is paired with the appropriately oriented $\boldsymbol{m}_{min}$. The system in this study does dynamically select different subsets of fiducials for different object poses because of occlusions of some of the markers. However, the operator cannot control this selection and optimal choice of fiducials for multiple POIs is not possible. Our study also shows that the direction along which the propagated uncertainty is the largest, corresponds to the eigenvector associated with the smallest eigenvalue of the covariance matrix of orientation data. However, this eigenvector is not aligned with the axis of the largest moment of inertia, i.e. the angle between the eigenvector and the axis of moment of inertia varies greatly for different object orientations. The large variations of angle can be attributed to the misalignment between the moment of inertia axes and the eigenvectors of the covariance matrix of fiducial noise.

7. Conclusions

For most manufacturing applications, not all points on an object are of equal interest. If a given point is important, then the uncertainty propagated to that point should be minimized. For pose measuring systems that determine pose by measuring fiducials, this can be achieved by strategic placement of fiducials so that the moment of inertia axis, $\boldsymbol{m}_{min}$, is aligned with a vector pointing to that point. We expect systems that are trained to extract points on object will show similar results. Other systems which use different methods for pose determination (e.g., fitting point cloud to CAD model) will require further investigation.

References

[1] X. Jiang, A. Konno, and M. Uchiyama, "A Vision-Based Endpoint Trajectory and Vibration Control for Flexible Manipulators," Int. Conference on Robotics and Automation ICRA, Roma, 2007.

[2] L. M. Brignone and M. Howarth, "A Geometrically Validated Approach to Autonomous Robotic Assembly," IEEE/RSJ Int. Conference on Intelligent Robots and Systems IROS, 2002.
[3] M. Prats, P. Martinet, A. P. Pobil, and S. Lee, "Robotic execution of everyday tasks by means of external vision/force control," *Inteligent Service Robotics,* vol. 1, no. 3, pp. 253-266, 2008.
[4] S. Huang, Y. Yamakawa, T. Senoo, and M. Ishikawa, "A Direct Visual Servo Scheme Based on Simplified Interaction Matrix for High-Speed Manipulation," Int. Conference on Robotics and Biomimetics, Guangzhou, China, 2012.
[5] H. Park, J. H. Bae, J. H. Park, M. H. Baeg, and J. Park, "Intuitive Peg-in-Hole Assembly Strategy with a Compliant Manipulator," 44th International Symposium on Robotics, 2013.
[6] H. Qiao and S. K. Tso, "Three-step precise robotic peg-hole insertion operation with symmetric regular polyhedral objects," *Int. J. Production Reserach,* vol. 37, no. 15, pp. 3541-3563, 1999.
[7] Z. Liu, Y. Xie, J. Xu, and K. Chen, "Laser tracker based robotic assembly system for large scale peg-hole parts," Int. Conference on Cyber Technology in Automation, Control and Intelligent Systems, Hong Kong, China, 2014.
[8] D. I. Park, C.Park, H. Do, T. Choi, and J. H. Kyung, "Assembly phase estimation in the square peg assembly process," Int. Conference on Control, Automation and Systems, Jeju, Korea, 2012.
[9] S. Chhatpar and M. S. Branicky, "Localization for Robotic Assemblies with Position Uncertainty," IEEE/RSJ Int. Conference on Intelligent Robots and Systems IROS, 2003.
[10] S. Chhatpar and M. S. Branicky, "Search Strategies for Peg-in-Hole Assemblies with Position Uncertainty," IEEE/RSJ Int. Conference on Intelligent Robots and Systems IROS, 2001.
[11] J. Y. Kim, W. S. Kim, and H. S. Cho, "Misalignment estimation and compensation for robotic assembly with uncertainty," *Robotica,* vol. 23, no. 03, pp. 355-364, 2005.
[12] R. Usubamatov and K. W. Leong, "Analyses of peg-hole jamming in automatic assembly machines," *Assembly Automation,* vol. 31, no. 4, pp. 358-362, 2011.
[13] R. Usubamatov, S. A. Adam, and A. Harun, "Analyzing the jamming of parts on the shaft in assembly processes," *Assembly Automation,* vol. 32, no. 4, pp. 340-346, 2012.
[14] M. Franaszek, M. Shah, G. S. Cheok, and K. S. Saidi, "The Axes of Random Infinitesimal Rotations and the Propagation of Orientation Uncertainty," *Measurement,* vol. 72, pp. 68-76, 2015.
[15] J. M. Fitzpatrick, J. B. West, and C. R. Maurer, "Predicting Error in Rigid-Body Point-Based Registration," *IEEE Trans. Medical Imaging,* vol. 17, no. 5, pp. 694 -702, 1998.
[16] R. R. Shamir, L. Joskowicz, and Y. Shoshan, "Fiducial Optimization for Minimal Target Registration Error in Image-Guided Neurosurgery," *IEEE Trans. Medical Imaging,* vol. 31, no. 3, pp. 725-737, 2012.
[17] J. B. West, J. M. Fitzpatrick, S. A. Toms, C. R. Maurer, and R. J. Maciunas, "Fiducial Point Placement and the Accuracy of Point-based, Rigid Body Registration," *Neurosurgery,* vol. 48, no. 4, pp. 810-817, 2001.
[18] A. Seginer, "Rigid-body point-based registration: The distribution of the target registration error when the fiducial registration errors are given," *Medical Image Analysis,* vol. 15, pp. 397-413, 2011.
[19] M. H. Moghari and P. Abolmaesumi, "Distribution of Target Registration Error for Anisotropic and Inhomogeneous Fiducial Localization Error," *IEEE Trans. Medical Imaging,* vol. 28, no. 6, pp. 799-813, 2009.
[20] G. S. Watson, "Distributions on the Circle and Sphere," *J. Applied Probability,* vol. 19, pp. 265-280, 1982.
[21] J. T. Kent, "The Fisher-Bingham Distribution on the Sphere," *J. Royal Statist. Soc. B,* vol. 44, no. 1, pp. 71-80, 1982.
[22] C. Bingham, "An antipodally symmetric distribution on the sphere," *The Annals of Statistics,* vol. 2, no. 6, pp. 1201-1225, 1974.
[23] A. D. Wiles, A. Likholyot, D. D. Frantz, and T. M. Peters, "A Statistical Model for Point-Based Target Registration Error With Anisotropic Fiducial Localizer Error," *IEEE Trans. Medical Imaging,* vol. 27, no. 3, pp. 378-390, 2008.
[24] Disclaimer: certain trade names and company products are mentioned in the text or identified in an illustration in order to adequately specify the experimental procedure and equipment used. In no case does such an identification imply recommendation or endorsement by the National Institute of Standards and Technology, nor does it imply that the products are necessarily the best available for the purpose.
[25] M. Moakher, "Means and Averaging in the Group of Rotations," *SIAM J.Matrix Analysis and Applications,* vol. 24, no. 1, pp. 1-16, 2002.
[26] K. S. Arun, T. S. Huang, and S. D. Blostein, "Least-Squares Fitting of Two 3-D Point Sets," *IEEE Trans. PAMI,* vol. 9, no. 5, pp. 698-700, 1987.